

The formation of globular clusters with top-heavy initial mass functions

Hajime Fukushima¹*, Hidenobu Yajima¹

¹Center for Computational Sciences, University of Tsukuba, Ten-nodai, 1-1-1 Tsukuba, Ibaraki 305-8577, Japan

Accepted XXX. Received YYY; in original form ZZZ

arXiv:2303.12405v2 [astro-ph.GA] 27 Jun 2023

ABSTRACT

We study the formation of globular clusters in massive compact clouds with the low-metallicity of $Z = 10^{-3} Z_{\odot}$ by performing three-dimensional radiative-hydrodynamics simulations. Considering the uncertainty of the initial mass function (IMF) of stars formed in low-metallicity and high-density clouds, we investigate the impacts of the IMF on the cloud condition for the GC formation with the range of the power-law index of IMF as $\gamma = 1 - 2.35$. We find that the threshold surface density (Σ_{thr}) for the GC formation increases from $800 M_{\odot} \text{ pc}^{-2}$ at $\gamma = 2.35$ to $1600 M_{\odot} \text{ pc}^{-2}$ at $\gamma = 1.5$ in the cases of clouds with $M_{\text{cl}} = 10^6 M_{\odot}$ because the emissivity of ionizing photons per stellar mass increases as γ decreases. For $\gamma < 1.5$, Σ_{thr} saturates with $\sim 2000 M_{\odot} \text{ pc}^{-2}$ that is quite rare and observed only in local starburst galaxies due to e.g., merger processes. Thus, we suggest that formation sites of low-metallicity GCs could be limited only in the very high-surface density regions. We also find that Σ_{thr} can be modelled by a power-law function with the cloud mass (M_{cl}) and the emissivity of ionizing photons (s_*) as $\propto M_{\text{cl}}^{-1/5} s_*^{2/5}$. Based on the relation between the power-law slope of IMF and Σ_{thr} , future observations with e.g., the James Webb Space Telescope can allow us to constrain the IMF of GCs.

Key words: stars:formation - stars:massive - stars:Population II - HII regions - galaxies: star clusters: general - galaxies: star formation.

1 INTRODUCTION

Globular clusters (GCs) are survivors of ancient star clusters born in the early Universe from the estimated age $\gtrsim 10$ Gyr (e.g., Portegies Zwart et al. 2010). GCs can be keys for understanding cosmic star formation rate and galaxy evolution in the early Universe. However, the formation mechanism of GCs has not been understood yet. Previous studies with cosmological simulations showed that massive and dense star clusters are formed in the early galaxies (Ricotti et al. 2016; Arata et al. 2018; McKenzie & Bekki 2021). In observations, Vanzella et al. (2017) discovered the young stellar system heavier than $10^5 M_{\odot}$ at $z \sim 6$ (see also Vanzella et al. 2019). Very recently, James Webb Space Telescope (JWST) has allowed us to probe massive and compact star clusters more precisely. Vanzella et al. (2022) discovered the star cluster whose stellar mass is comparable to GCs ($\sim 10^6 M_{\odot}$) at $z \sim 4$.

In the GC formation, efficient conversion from the gas to stars is a necessary condition. After evaporation of a star-forming cloud, the stellar density decreases significantly if the stellar system is gravitationally unbound. N -body simulations showed that more than 10–30 percent of the gas should be converted into stars to make the star cluster gravitationally bound state (e.g., Lada et al. 1984; Kroupa et al. 2001; Baumgardt & Kroupa 2007; Shukrgaliyev et al. 2017). Recent hydrodynamics simulations show that the bound fractions of star clusters are tightly related to the star formation efficiencies (SFEs) (Li et al. 2019; Grudić et al. 2021; Fukushima & Yajima 2022). In the Milky Way, the SFEs are typically less than 10 percent

(e.g., Myers et al. 1986; Chevance et al. 2020), and so most star clusters are dispersed after their birth (Lada & Lada 2003).

In star cluster formation, massive stars disrupt their host clouds with stellar feedback, such as radiative feedback, stellar wind, and supernovae (SNe) (e.g., Krumholz et al. 2019; Chevance et al. 2022). Extreme ultraviolet (EUV; $13.6 \text{ eV} \lesssim h\nu \lesssim 1 \text{ keV}$) photons ionize the hydrogen atoms and heat gas to 10^4 K of which the high thermal pressure can disrupt clouds (e.g., Williams & McKee 1997; Matzner 2002; Krumholz & Matzner 2009; Fall et al. 2010; Kim et al. 2016; Inoguchi et al. 2020). This photoionization feedback can regulate the SFEs to be less than ~ 0.1 in the environments of the Milky Way (e.g., Vázquez-Semadeni et al. 2010; Dale et al. 2012, 2013; Howard et al. 2017; Geen et al. 2017; Gavagnin et al. 2017; Kim et al. 2018; He et al. 2019; Decataldo et al. 2020; Grudić et al. 2018; Fukushima et al. 2020b; Grudić et al. 2021; González-Samaniego & Vazquez-Semadeni 2020; Bending et al. 2020; Ali 2021; Fujii et al. 2021; Dobbs et al. 2022; Kimm et al. 2022; Grudić et al. 2022). Stellar wind also injects kinetic energy into the ambient matters (Weaver et al. 1977). However, Lancaster et al. (2021a) showed that the mixing layers around the bubble efficiently lost energy, resulting in the weak impacts on the cloud disruption (see also Lancaster et al. 2021b,c). Supernova feedback is powerful enough to evacuate the gas from a cloud (e.g., Geen et al. 2016). Yet, recent observations indicate that clouds are disrupted before the end of the lifetime of OB stars (Kruisissen et al. 2019). Thus, photoionization is likely to play a primary role in the star cluster formation (Guszejnov et al. 2022). Note that the radiation pressure on dust grains also regulates the star formation (Murray et al. 2010; Skinner & Ostriker 2015;

* E-mail:fukushima@ccs.tsukuba.ac.jp

Raskutti et al. 2016). However, it should be secondary because of the low-metallicities of clouds hosting GCs.

In understanding the relationship between the photoionization feedback and the star cluster formation, the initial mass function (IMF) is an essential factor. The production rate of ionizing photons sensitively depends on the shape of the IMF. It is well known that the IMF in the nearby star-forming regions is universal (e.g. Salpeter 1955; Kroupa 2002; Chabrier 2003). Observations of massive star clusters indicated that the IMF is top-heavy in these highly dense clusters (Lu et al. 2013; Maia et al. 2016; Schneider et al. 2018; Hosek et al. 2019). The observed slopes of the IMFs are $\gamma = 1.7 - 1.9$, and there is an excess of massive stars. Pouteau et al. (2022) showed that the core mass function is shallower than the Salpeter IMF in the massive star-forming regions ($\gamma = 1.95$, W43-MM2&MM3). Besides, indirect evidence of the top-heavy IMF in GCs is also found (Marks et al. 2012). They found that the IMF of GCs with low-metallicities or high-stellar densities tends to be top-heavy. Using their results, Zonoozi et al. (2016) showed that the top-heavy IMF could nicely explain the relation between the mass-to-light ratios and metallicity of GCs in M31 (see also, Haghi et al. 2017). On the other hand, Baumgardt et al. (2023) indicated that there is no evidence of top-heavy IMFs in GCs of the Galaxy and the Large/Small Magellanic Clouds in the metallicity range of $Z > 10^{-2} Z_{\odot}$. Therefore, the IMF of low-metallicity GC is still under debate. In particular, the case with a metallicity lower than $\sim 10^{-2} Z_{\odot}$ is poorly understood.

Recently, Chon et al. (2021) performed hydrodynamics simulations, including the cooling effects of metal lines and dust grains. They showed that the highly filamentary structures are induced, and the Chabrier-like IMF (Chabrier 2003) is realized at $Z \gtrsim 10^{-1} Z_{\odot}$. In the low-metallicity environments with $Z \lesssim 10^{-2} Z_{\odot}$, the formation of the filamentary structures is suppressed, resulting in the top-heavy IMF. Also, Toyouchi et al. (2022) indicated that the IMF should be top-heavy with $\gamma < 1$ around the active galactic nuclei to reproduce the observed Fe II / Mg II line-flux ratio. Thus, the IMF is likely top-heavy in the low metallicity and the high gas density environments.

In this paper, we study the conditions of clouds for GC formation with top-heavy IMFs. We consider clouds with masses of $M_{\text{cl}} = 10^6$ and $10^7 M_{\odot}$ and the cloud surface densities of $\Sigma_{\text{cl}} \sim 400 - 2000 M_{\odot} \text{pc}^{-2}$. We utilize the 3D radiative-hydrodynamics (RHD) simulation code, SFUMATO-M1 which is the modified code of a self-gravitational magnetohydrodynamics code with an Eulerian adaptive mesh refinement (AMR), SFUMATO (Matsumoto 2007; Matsumoto et al. 2015). We adopt the radiation transfer scheme based on the momentum method with the M1-closure and the stochastic stellar population developed in Fukushima & Yajima (2021, hereafter Paper I) and Fukushima & Yajima (2022).

We organize the rest of this paper as the following. In Section 2, we describe the numerical method and the initial conditions of the simulations. Then, we show the results of the simulations in Section 3. In Section 4, we discuss the implications of our simulations on the low-metallicity GC formation. Section 5 is for the summary.

2 SIMULATION METHOD

We perform the RHD simulations with SFUMATO-M1 (Paper I), the modified version of self-gravitational magnetohydrodynamics code SFUMATO (Matsumoto 2007) which utilizes the adaptive mesh refinement technique. Our simulations include on-the-fly radiative transfer calculations with the M1-closure technique. As in Rosdahl et al. (2013), we adopt the approximation with the reduced speed of

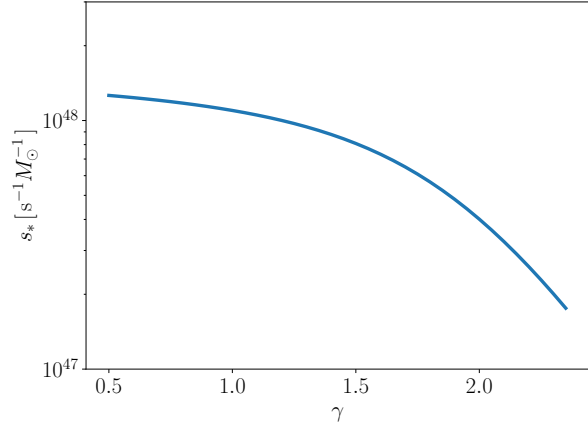


Figure 1. The emissivity of ionizing photons as a function of the slope of the stellar IMF.

light for the radiation transfer with $\tilde{c} = 3 \times 10^{-4} c$ where c is the speed of light. We set the four frequency bins for (1) extreme ultraviolet ($13.6 \text{ eV} < h\nu$), (2) Lyman-Werner ($11.2 \text{ eV} < h\nu < 13.6 \text{ eV}$), (3) far-ultraviolet ($6 \text{ eV} < h\nu < 13.6 \text{ eV}$), and (4) infrared photons. The chemistry solver is developed in Sugimura et al. (2020) which studied the primordial star formation. We added the chemical network of CO and the oxygen ion in the HII regions (OII and OIII, Fukushima et al. 2020a). We also adopt the sink particle technique for modelling a star cluster as in Matsumoto et al. (2015). Further detail of the simulation methods is described in Paper I and Fukushima & Yajima (2022). In this study, we fixed the metallicity at $Z = 10^{-3} Z_{\odot}$.

2.1 Model of stellar population

We adopt the stochastic stellar population model developed in Fukushima & Yajima (2022). This model is similar to SLUG code developed by da Silva et al. (2012) and Krumholz et al. (2015). We divide the masses into 150 bins between 0.1 and $300 M_{\odot}$. In the Milky way, it is known that there is an upper limit in stellar mass around $150 M_{\odot}$ (Weidner & Kroupa 2004; Figer 2005). However, a massive star whose initial mass is more than $\sim 200 M_{\odot}$ was discovered in the R136 star cluster in the Large Magellanic Cloud (Crowther et al. 2010; Kalari et al. 2022). The upper stellar mass in the GCs is still unknown. Thus, we adopt $300 M_{\odot}$ as the upper stellar mass limit. The newborn stars are stochastically distributed into bins based on the probability from the IMF. We adopt the Chabrier IMF (Chabrier 2003) but change the slope of the massive end. In the standard IMF, the slope is $\gamma = 2.35$ as the Salpeter IMF (Salpeter 1955), where the number of stars within a specific mass range is $dn \propto m^{-\gamma} dm$. Figure 1 shows the emissivity of ionizing photons per unit stellar mass averaged over the IMF as a function of γ . The shape of the IMF in a low-metallicity massive star cluster is still unknown. Chon et al. (2021) indicated that the slope of IMF is shallower than $\gamma = 2$. Thus, we mainly consider the case with $\gamma = 1.5$ as the fiducial model of the top-heavy IMF. Besides, we calculate the models with $\gamma = 1$ and 2. In the low-mass star clusters ($M_* < 10^4 M_{\odot}$), the emissivity is not uniform due to the stochastic stellar population (Kim et al. 2016) even if the total stellar mass is same. However, the total stellar masses in our simulations are larger than $10^4 M_{\odot}$. Therefore, the radiative properties of GCs are almost the same as the IMF averaged values.

Table 1. Models considered.

model	M_{cl} [M_{\odot}]	Σ_{cl} [$M_{\odot}\text{pc}^{-2}$]	R_{cl} [pc]	γ	t_{ff} [Myr]	v_{esc} [km/s]
M6R125G15	10^6	2000	12.5	1.5	0.73	26
M6R13G1	10^6	2000	13	1	0.74	26
M6R135G15	10^6	1700	13.5	1.5	0.82	25
M6R14G15	10^6	1600	14	1.5	0.87	25
M6R15G15	10^6	1400	15	1.5	0.96	24
M6R14G1	10^6	1700	14	1	0.84	25
M6R16G2	10^6	1300	16	2	1.0	23
M6R18G2	10^6	1000	18	2	1.2	22
M6R19G2	10^6	900	19	2	1.3	21
M6R20G15	10^6	800	20	1.5	1.5	21
M6R20G235	10^6	800	20	2.35	1.5	21
M6R23G235	10^6	600	23	2.35	1.8	19
M6R28G235	10^6	410	28	2.35	2.5	18
M7R46G15	10^7	1500	46	1.5	1.6	43
M7R50G15	10^7	1300	50	1.5	1.9	41
M7R56G15	10^7	1000	56	1.5	2.2	39
M7R63G15	10^7	800	63	1.5	2.6	37
M7R63G235	10^7	800	63	2.35	2.6	37
M7R73G235	10^7	600	73	2.35	3.3	34
M7R89G235	10^7	400	89	2.35	4.4	31

Notes. Column 1: model names, Column 2: cloud masses, Column 3: cloud radii, Column 4: surface densities, Column 5: high-mass IMF slope, Column 6: free-fall times, Column 7: escape velocities.

The stars are distributed in each sink particle at different times, and their radiative properties depend on their ages. We consider the stellar evolution to estimate their radiative properties by adopting the PARSEC tracks (Bressan et al. 2012; Tang et al. 2014; Chen et al. 2014, 2015; Marigo et al. 2017; Pastorelli et al. 2019, 2020). The lower metallicity limit of PARSEC tracks is $Z = 10^{-2} Z_{\odot}$, and thus we adopt the stellar evolution track at this value. In addition, we use the SED models in Lejeune et al. (1997) and Hainich et al. (2019) for OB-stars in SMC to calculate the emissivity of ionizing photons. We note that the typical mass ranges of sink particles are $10^2 - 10^4 M_{\odot}$ ($10^3 - 10^5 M_{\odot}$), and its mean values are $\sim 10^3 M_{\odot}$ ($\sim 10^4 M_{\odot}$) with the cloud mass $10^6 M_{\odot}$ ($10^7 M_{\odot}$) in our simulations.

2.2 Initial condition

We perform the simulations of clouds with the masses $M_{\text{cl}} = 10^6 M_{\odot}$ and $10^7 M_{\odot}$. We change the slopes of the IMF as $\gamma = 1, 1.5, 2$, and 2.35 . By considering the variety of initial states of the clouds, we investigate the cases with $\Sigma_{\text{cl}} = 400 - 2000 M_{\odot}\text{pc}^{-2}$. The models are summarized in Table 1. Hereafter, we label models according to which the cloud mass (M_{cl}), the radius (R_{cl}), and the slope of the IMF (γ). For example, "M6R20G235" represents the model with $M_{\text{cl}} = 10^6 M_{\odot}$, $R_{\text{cl}} = 20$ pc, and $\gamma = 2.35$. In each simulation, the maximum refinement level is fixed at $l_{\text{max}} = 4$. The minimum cell size is $\Delta x = 0.059 \text{ pc}(R_{\text{cl}}/20 \text{ pc})$ where R_{cl} is the cloud radius. Our simulations can resolve compact HII regions in high-density regions in a cloud sufficiently. As in Paper I, we set the turbulent motions in the initial condition with the velocity power spectrum as $P(k) \propto k^{-4}$ where k is the wavenumber. The strength of the turbulent motions is characterized by the virial parameter defined as

$$\alpha_0 = \frac{2E_{\text{kin}}}{|E_{\text{grav}}|} = \frac{5\sigma_0^2 R_{\text{cl}}}{3GM_{\text{cl}}}, \quad (1)$$

Table 2. Simulation results.

model	ε_*	M_{pd} [M_{\odot}]	f_{bd}	r_{h} [pc]	ρ_* [$M_{\odot}\text{pc}^{-3}$]
M6R125G15	0.40	3.9×10^5	0.98	0.22	9.1×10^6
M6R13G1	0.18	1.3×10^5	0.73	1.8	5.2×10^3
M6R135G15	0.31	3.0×10^5	0.96	0.48	6.5×10^5
M6R14G15	0.18	1.3×10^5	0.74	1.9	4.7×10^3
M6R15G15	0.15	7.8×10^4	0.53	3.4	5.0×10^2
M6R14G1	0.13	5.0×10^4	0.38	2.8	5.7×10^2
M6R16G2	0.39	3.8×10^5	0.98	0.31	3.0×10^6
M6R18G2	0.19	1.6×10^5	0.84	2.8	1.7×10^3
M6R19G2	0.16	1.2×10^5	0.75	3.8	5.1×10^2
M6R20G15	0.078	8.2×10^3	0.11	1.5	6.3×10^2
M6R20G235	0.49	4.8×10^5	0.99	0.39	2.0×10^6
M6R23G235	0.17	1.2×10^5	0.73	5.1	2.2×10^2
M6R28G235	0.11	2.6×10^4	0.23	6.8	1.9×10^1
M7R46G15	0.48	4.5×10^6	0.99	0.91	1.4×10^6
M7R50G15	0.32	2.9×10^6	0.96	1.3	3.5×10^5
M7R56G15	0.11	5.9×10^5	0.54	12.0	7.8×10^1
M7R63G15	0.076	8.3×10^4	0.11	2.2	2.4×10^3
M7R63G235	0.60	5.8×10^6	1.0	1.4	4.6×10^5
M7R73G235	0.45	4.4×10^6	0.99	1.9	1.6×10^5
M7R89G235	0.13	5.6×10^5	0.43	19.0	1.9×10^1

Notes. Column 1: model names, Column 2: star formation efficiencies, Column 3: gravitationally bound masses, Column 4: gravitational bound fraction of star clusters, Column 5: half-mass radii, Column 6: stellar densities of star clusters.

where σ_0 , E_{kin} , and E_{grav} are the 3D velocity dispersion, kinetic and gravitational energy. Here, we adopt $\alpha_0 = 1$.

3 RESULTS

We first represent the impact of the top-heavy IMF on the dense star cluster formation in Section 3.1. In Section 3.2, we investigate the condition for the formation of dense star clusters. In Table 2, we summarize the results of our simulations.

3.1 Star cluster formation with top-heavy IMF

We present the star cluster formation in the case of the models with $(M_{\text{cl}}, \Sigma_{\text{cl}}) = (10^6 M_{\odot}, 800 M_{\odot})$. Figure 2 shows the time evolution of the gas surface densities with the top-heavy IMF ($\gamma = 1.5$) and the standard IMF ($\gamma = 2.35$). The entire evolution is almost the same until the elapsed time $t \sim 1.0 t_{\text{ff}}$ where t_{ff} is the free-fall time of the cloud. Once a few percent of gas is converted into stars ($t \sim 1.5 t_{\text{ff}}$), gas clumps around stars start to be evacuated only in the case of the top-heavy IMF. As a result, the gravitational potential is too shallow to bind the star cluster compactly, allowing the expansion of stellar distribution. In this case, the star cluster has a stellar mass density lower than that of GCs. On the other hand, in the case of the standard IMF, gas inflow and star formation continue against the stellar feedback even at $t \gtrsim 1.5 t_{\text{ff}}$. Finally, the compact star cluster form at the center of the cloud, and its density is comparable to the observed GCs.

Figure 3 shows the time evolution of the stellar mass and density in each model. Here, we calculate the total mass and half-mass radius of the bound stars to obtain the stellar densities. The details of the analytical method are described in Paper I. The photoionization feedback suppresses the star formation significantly in the case of the top-heavy IMF ($\gamma = 1.5$). The star formation efficiency (SFE) results

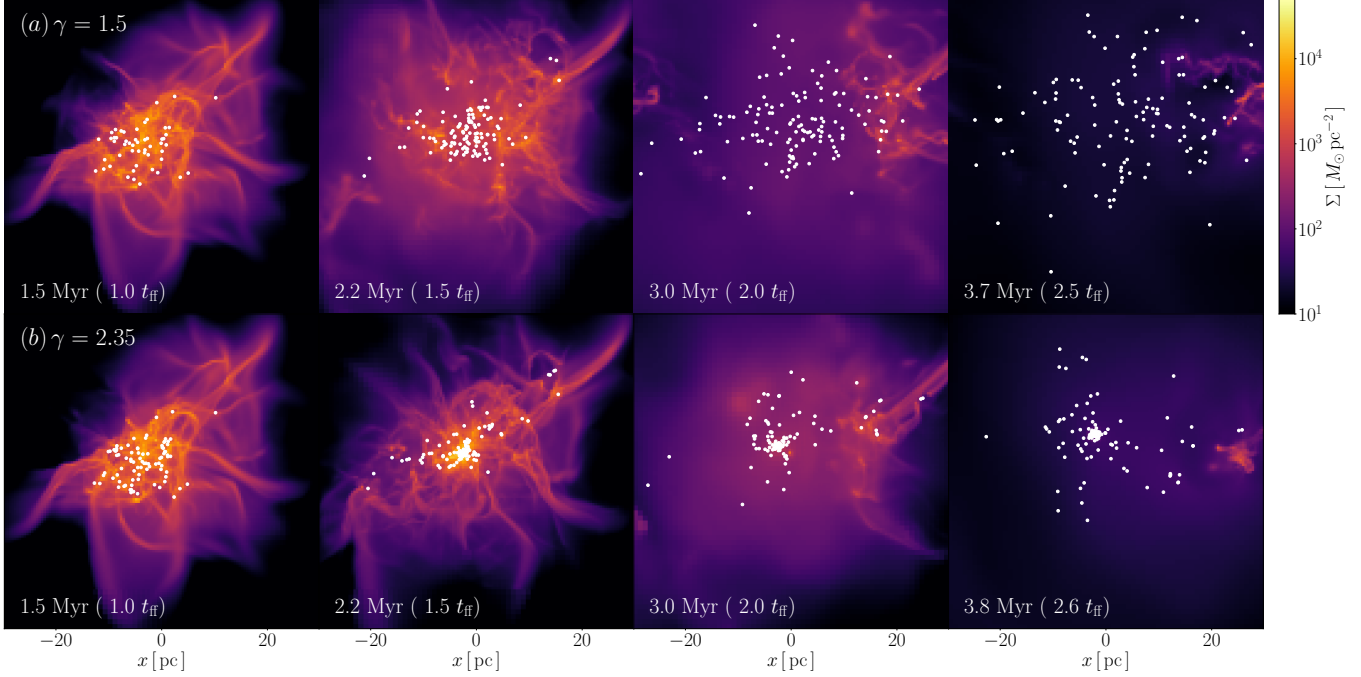


Figure 2. Star cluster formation and cloud dispersion in the clouds with $M_{\text{cl}} = 10^6 M_{\odot}$ and $\Sigma_{\text{cl}} = 800 M_{\odot}\text{pc}^{-2}$. The panels show the evolution of the surface densities. The top and bottom rows show the models with $\gamma = 1.5$ and 2.35 . The white dots represent the positions of stellar particles.

in less than 10 percent. In such a case, the stars are not bound by their own gravitational potential. Thus, the resultant stellar density is lower than $10^3 M_{\odot}\text{pc}^{-3}$.

In the case of the standard IMF ($\gamma = 2.35$), the star formation rate steeply increases at $t \gtrsim 1.3 t_{\text{ff}}$. In this phase, the high-density and gravitationally bound stellar core forms. Finally, more than 40 percent of the gas is converted into stars, resulting in a massive compact star cluster. The stellar density shows $\sim 10^6 M_{\odot}\text{pc}^{-3}$ which is similar to GCs. We note that most gravitationally bound stars belong to the stellar cores. The density of the stellar core is almost the same as that of a star cluster, as shown in Table 2.

3.2 Dependence on IMF

The large differences in the SFE and the stellar density are related to the stellar core formation as shown in Figure 2. If the gas accretion continues against the photoionization feedback, the high-density stellar core forms at the center of the cloud. In Paper I, we analytically derive the threshold surface density for the stellar core formation as

$$\Sigma_{\text{cl}} > \Sigma_{\text{thr}} = 670 M_{\odot}\text{pc}^{-2} \left(\frac{M_{\text{cl}}}{10^6 M_{\odot}} \right)^{-1/5} \left(\frac{s_*}{10^{47} M_{\odot}^{-1}\text{s}^{-1}} \right)^{2/5}, \quad (2)$$

where s_* is the number of ionizing photons per unit stellar mass. Here, we consider the expanding shell model as in Matzner (2002) and Krumholz & Matzner (2009). The deviation of Σ_{thr} is shown in Appendix A. The cloud of $(M_{\text{cl}}, \Sigma_{\text{cl}}) = (10^6 M_{\odot}, 800 M_{\odot}\text{pc}^{-2})$ satisfies this condition with the standard IMF. However, the threshold surface density increases up to $\Sigma_{\text{cl}} > 1600 M_{\odot}\text{pc}^{-2}$ in the case of the top-heavy IMF ($\gamma = 1.5$). Therefore, the massive and high-dense star clusters are difficult to form as the IMF is top-heavy.

Figure 4 shows the dependencies of SFEs and the stellar densities

on the surface density in the cases with the various cloud masses ($M_{\text{cl}} = 10^6 M_{\odot}$ and $10^7 M_{\odot}$) and the slope of the IMF ($\gamma = 1.5$ and 2.35) as Table 1. We estimate these values when the elapsed time of the simulations is $t = 2 t_{\text{ff}}$. The SFE and the stellar densities increase with the higher surface densities. The stellar core formation occurs when the SFE typically exceeds 0.15–0.2. In such a case, the bound mass and the stellar densities are higher than $10^5 M_{\odot}$ and $> 10^5 M_{\odot}\text{pc}^{-3}$ which are similar to the properties of observed GCs. With the top-heavy IMF ($\gamma = 1.5$), the core formation occurs at $\Sigma_{\text{cl}} > 1600 M_{\odot}\text{pc}^{-2}$ ($1000 M_{\odot}\text{pc}^{-2}$) in the clouds with $M_{\text{cl}} = 10^6 M_{\odot}$ ($10^7 M_{\odot}$). In the case with the standard IMF ($\gamma = 2.35$), the threshold surface density decreases to $\Sigma_{\text{thr}} = 750 M_{\odot}\text{pc}^{-2}$ ($470 M_{\odot}\text{pc}^{-2}$) with $M_{\text{cl}} = 10^6 M_{\odot}$ ($10^7 M_{\odot}$) due to the decrease of the emissivity of the ionizing photons. These results are consistent with the threshold surface density given as Equation (2).

To investigate the dependency of the IMF slope on Σ_{thr} , we additionally perform the models with $\gamma = 1$ and 2 as Table 1. Figure 5 shows the numerical results of the stellar densities in the plane of γ and Σ_{cl} with the cloud mass of $M_{\text{cl}} = 10^6 M_{\odot}$. The triangles and circles represent the cases where the star cluster satisfies the properties of GC progenitors ($M_{\text{bh}} > 10^5 M_{\odot}$ and $\rho_* > 10^3 M_{\odot}\text{pc}^{-3}$, Portegies Zwart et al. 2010). Some GCs in the Milky Way have lower stellar density than this threshold value. However, star clusters gradually expand with time after their birth (e.g., Pfalzner 2009; Fujii & Portegies Zwart 2016). Therefore, the stellar density $10^3 M_{\odot}\text{pc}^{-3}$ can be reasonable condition for the GC formation. The threshold surface density Σ_{thr} derived in the analytical model (eq. 2) reproduces the simulation results well. The threshold value is $750 M_{\odot}\text{pc}^{-2}$ for $\gamma = 2.35$, and it increases as γ decreases. At $\gamma \lesssim 1.5$, the threshold surface density is not sensitive to γ because s_* does not change with γ significantly. Thus, we suggest that once a high-density cloud with $\Sigma \gtrsim 2 \times 10^3 M_{\odot}\text{pc}^{-2}$ forms, GCs are likely to form even if the IMF is top-heavy ($\gamma = 1.5$).

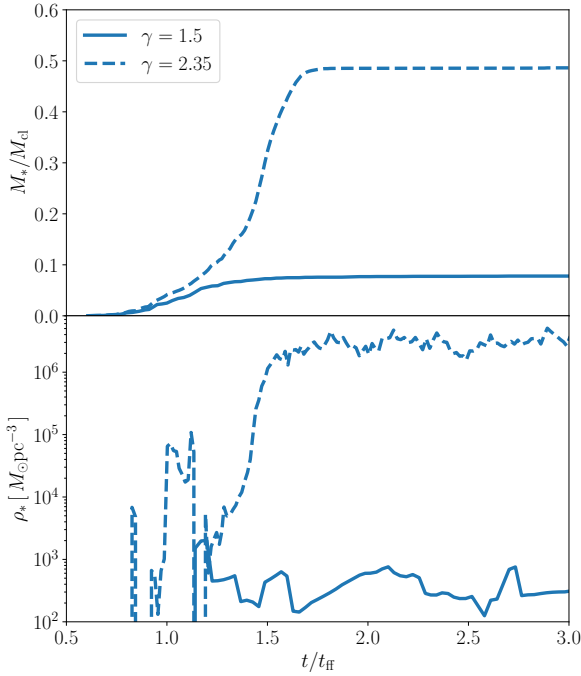


Figure 3. Upper panel: the time evolution of the stellar mass in the cases with $(M_{\text{cl}}, \Sigma_{\text{cl}}) = (10^6 M_{\odot}, 800 M_{\odot} \text{pc}^{-2})$. Lower panel: the time evolution of the stellar density. Each line represents the different IMF with $\gamma = 1.5$ (solid) and 2.35 (dashed line).

4 DISCUSSION

In this paper, we study the impacts of the IMF on the condition for GC formation in low-metallicity clouds. The observations of the GCs in the Milky Way showed that there is the metallicity floor at $Z \sim 10^{-2.5} Z_{\odot}$ (e.g., Puzia et al. 2005; Beasley et al. 2019). This metallicity floor can be related to the formation sites and mechanisms of GCs. Kruijssen (2019) indicated that the metallicity floor results from the mass-metallicity relation of their host galaxies. They showed that the galaxies with metallicities less than the floor are too small to form GCs. Abe & Yajima (2018) pointed out that radiation pressure caused by the Ly α photons suppresses the bound star cluster in the low-metallicity environments ($Z \lesssim 10^{-2.5} Z_{\odot}$). We suggested that more compact clouds ($\Sigma_{\text{cl}} > 10^3 M_{\odot} \text{pc}^{-2}$) are necessary for the GC formation at $Z \lesssim 10^{-3} Z_{\odot}$ if the IMF is a top-heavy (Chon et al. 2021). In such high surface density environments, the formed bound star cluster is more likely to be destroyed due to the interactions with another star-forming cloud (e.g., Spitzer 1987; Kundic & Ostriker 1995; Gieles et al. 2006; Gnedin et al. 1999; Kruijssen 2012). Besides, the star clusters with the top-heavy IMF cannot survive for a long time (e.g., Wang et al. 2020, 2021). In such a star cluster, more remnant black holes (BHs) form and migrate to the center by kicking neighbor low-mass stars. These star clusters can be finally evaporated or become dark star clusters that only contain BHs (Banerjee & Kroupa 2011). On the other hand, observations have discovered the GCs with metallicities lower than the metallicity floor in most GCs (e.g., Larsen et al. 2020; Wan et al. 2020; Martin et al. 2022). Therefore, further studies are needed to connect the formation of

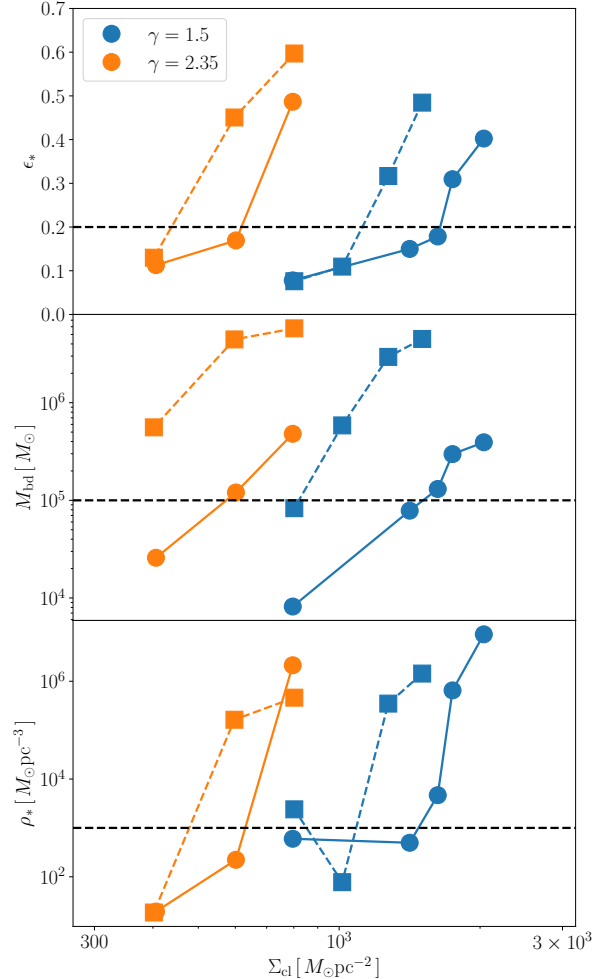


Figure 4. Upper panel: SFEs of clouds as a function of surface densities. The back dashed line represents $\epsilon_* = 0.2$. Lower panel: Stellar densities of star clusters. Each symbol represents the different cloud masses: $M_{\text{cl}} = 10^6 M_{\odot}$ (circle) and $10^7 M_{\odot}$ (square). Each color shows the slope of the IMF: $\gamma = 1.5$ (blue) and 2.35 (orange).

low-metallicity GCs, their stellar IMF, and their survival rates in the early galaxies.

The formation sites of young massive star clusters have been observed frequently in the starburst and merger galaxies (e.g., Leroy et al. 2018; Tsuge et al. 2021). The numerical simulations have indicated massive clouds could be induced with galaxy merger processes (e.g., Arata et al. 2018; Lahén et al. 2019). In these environments, the colliding flow with thermal or gravitational instability can be key to forming massive compact clouds (Inoue & Inutsuka 2012; Kobayashi et al. 2020; Maeda et al. 2021; Dobbs et al. 2020, 2022). The above large-scale conditions can determine the initial condition of clouds as used in our work. We will connect the global structure in a galaxy and the star cluster formation in a cloud in future work.

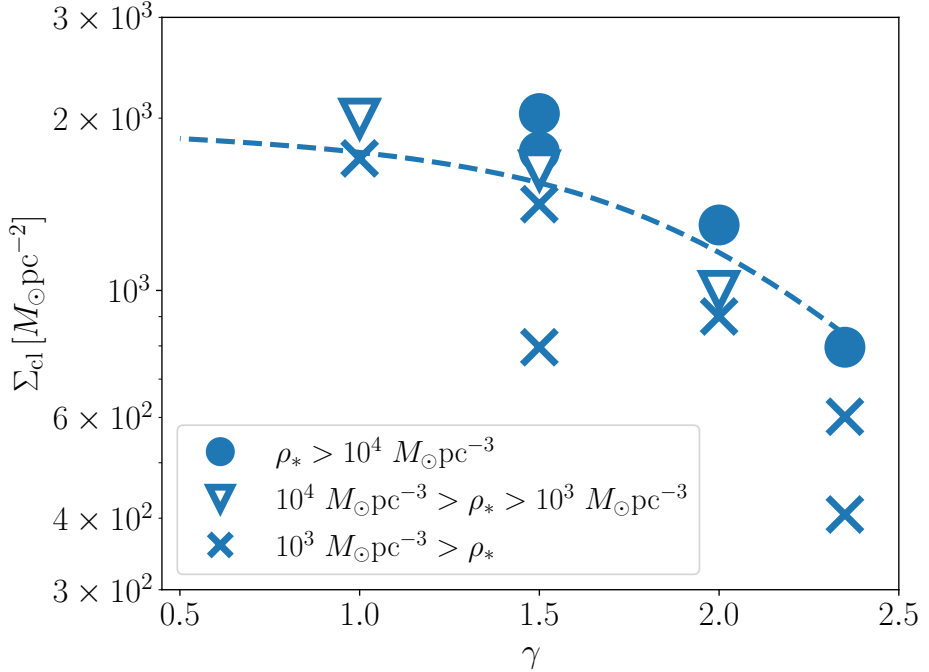


Figure 5. The threshold surface density (Σ_{thr}) for GC formation with $M_{cl} = 10^6 M_\odot$ as a function of the slope of the IMF (γ). The dashed line shows the analytical result given as Eq. (2). The symbols indicate the stellar densities of star clusters. The circles, triangles, and crosses correspond to the cases with $\rho_* > 10^4 M_\odot pc^{-3}$, $10^4 M_\odot pc^{-3} > \rho_* > 10^3 M_\odot pc^{-3}$, and $10^3 M_\odot pc^{-3} > \rho_*$, respectively. In the cases of triangles and circles, the bound stellar mass exceeds $10^5 M_\odot$.

In this work, we do not include the effects of magnetic fields. Recent numerical studies have shown that magnetic fields have crucial roles, even in the first star formation (e.g., Sharda et al. 2020, 2021; Stacy et al. 2022; Sadanari et al. 2021; Stacy et al. 2022; Sadanari et al. 2023). Strong magnetic fields suppress star formation and decrease star formation efficiencies and rates in star cluster formation (e.g., Kim et al. 2021). The expansion velocity of HII regions can be lower with lower star formation rates. Thus, GCs can be born in a cloud with lower surface density (see also Appendix A). However, note that, if the duration of star formation is longer than the lifetime of massive stars, supernova feedback can suppress the GC formation. For further studies, we will include magnetic fields in future works.

We investigate the cases with $Z = 10^{-3} Z_\odot$ in this paper. At $Z \lesssim 10^{-2} Z_\odot$, the temperature of HII regions does not change significantly (e.g., Draine 2011), and dust attenuation of UV photons is inefficient even for high-density filamentary structures (Fukushima et al. 2020b). Therefore, the GC formation is unlikely to be sensitive to the metallicity at $Z \lesssim 10^{-2} Z_\odot$. On the other hand, the temperature of ionizing gas decreases, and filaments are shielded by dust grains at higher metallicities. In such a case, the photoionization feedback is slightly more ineffective in suppressing star formation. In addition, Menon et al. (2022) showed that infrared radiation pressure does not sufficiently decrease star formation efficiency even at solar metallicity. Therefore, GCs can form more frequently in clouds with higher metallicity.

5 SUMMARY

We have performed three-dimensional radiative-hydrodynamics simulations of the formation of the low-metallicity globular clusters (GCs) with $Z = 10^{-3} Z_\odot$. We have investigated the impacts of different initial mass functions (IMFs) on the properties of emergent star clusters. Our simulations cover the various cloud masses and surface densities, $M_{cl} = 10^6 - 10^7 M_\odot$ and $\Sigma_{cl} = 400 - 2000 M_\odot pc^{-2}$. Our findings are summarized as follows:

(i) GCs form only in compact clouds with $\Sigma_{cl} \sim 800 M_\odot pc^{-2}$ for the cloud mass $M_{cl} = 10^6 M_\odot$ in the case of standard Salpeter-like IMF ($\gamma = 2.35$). With the top-heavy IMF of $\gamma = 1.5$, the threshold surface density (Σ_{thr}) increases up to $\Sigma_{thr} \sim 1600 M_\odot pc^{-2}$ due to the higher emissivity of ionizing photons per unit stellar mass. For $\gamma < 1.5$, Σ_{thr} saturates with $\Sigma_{thr} \sim 2000 M_\odot pc^{-2}$ because of saturation of the photon emissivity.

(ii) The simulation results about the threshold surface densities are reproduced well by a semi-analytical model updated from that derived in Fukushima & Yajima (2021). The threshold surface density mainly depends on the cloud mass and the emissivity of ionizing photons (s_*) as $\Sigma_{cl} \propto M_{cl}^{-1/5} s_*^{2/5}$.

Theoretical studies predicted that GCs formed in dwarf galaxies in the early Universe (e.g., Ricotti et al. 2016; McKenzie & Bekki 2021) due to the high Jeans mass (Peebles & Dicke 1968), or thermal instability in low-metallicity gas (Fall & Rees 1985; Arata et al. 2018). The collapse of the clouds under UV background radiation also induces the GC formation (Hasegawa et al. 2009; Abe et al. 2016). Thanks to JAMES WEBB SPACE TELESCOPE (JWST), star-formation sites in high-redshift galaxies have been observed directly (e.g., Vanzella et al.

2022). Also, recent observations suggested the physical properties of the gas, e.g., density, temperature, and metallicity in star-forming regions of high-redshift galaxies (e.g., Isobe et al. 2023). Combining the GC formation condition obtained in this study with the observations, we will study the origin of GCs in future work. Recently, Inayoshi et al. (2022) indicated that star-formation efficiencies (SFEs) can be higher than $\sim 0.1 - 0.3$ in galaxies at $z > 10$ from observed UV luminosity functions (e.g., Harikane et al. 2022b,a; Finkelstein et al. 2022). These high SFEs satisfy a condition for the GC formation. With upcoming observations, we will study the GC formation at $z \gtrsim 10$ with cosmological simulations of galaxy formation (e.g., Abe et al. 2021; Yajima et al. 2022).

ACKNOWLEDGEMENTS

The authors wish to express their cordial thanks to Profs. Masayuki Umemura and Ken Ohsuga for their continual interest, advice, and encouragement. We appreciate Tomoaki Matsumoto for his great contribution to code development. We would like to thank Takashi Hosokawa for useful discussions and comments. The numerical simulations were performed on the Cray XC50 (Aterui II) at the Center for Computational Astrophysics of National Astronomical Observatory of Japan and Yukawa-21 at Yukawa Institute for Theoretical Physics at Kyoto University. This work is supported in part by MEXT/JSPS KAKENHI Grant Number 17H04827, 20H04724, 21H04489 (HY), NAOJ ALMA Scientific Research Grant Numbers 2019-11A, JST FOREST Program, Grant Number JP-MJFR202Z, and Astro Biology Center Project research AB041008 (HY).

DATA AVAILABILITY

The data underlying this article will be shared on reasonable request to the corresponding author.

REFERENCES

- Abe M., Yajima H., 2018, *MNRAS*, **475**, L130
 Abe M., Umemura M., Hasegawa K., 2016, *MNRAS*, **463**, 2849
 Abe M., Yajima H., Khochfar S., Dalla Vecchia C., Omukai K., 2021, *MNRAS*, **508**, 3226
 Ali A. A., 2021, *MNRAS*, **501**, 4136
 Arata S., Yajima H., Nagamine K., 2018, *MNRAS*, **475**, 4252
 Banerjee S., Kroupa P., 2011, *ApJ*, **741**, L12
 Baumgardt H., Kroupa P., 2007, *MNRAS*, **380**, 1589
 Baumgardt H., Henault-Brunet V., Dickson N., Sollima A., 2023, arXiv e-prints, p. arXiv:2303.01636
 Beasley M. A., Leaman R., Gallart C., Larsen S. S., Battaglia G., Monelli M., Pedreros M. H., 2019, *MNRAS*, **487**, 1986
 Bending T. J. R., Dobbs C. L., Bate M. R., 2020, *MNRAS*, **495**, 1672
 Bressan A., Marigo P., Girardi L., Salasnich B., Dal Cero C., Rubele S., Nanni A., 2012, *MNRAS*, **427**, 127
 Chabrier G., 2003, *PASP*, **115**, 763
 Chen Y., Girardi L., Bressan A., Marigo P., Barbieri M., Kong X., 2014, *MNRAS*, **444**, 2525
 Chen Y., Bressan A., Girardi L., Marigo P., Kong X., Lanza A., 2015, *MNRAS*, **452**, 1068
 Chevance M., et al., 2020, *MNRAS*, **493**, 2872
 Chevance M., Krumholz M. R., McLeod A. F., Ostriker E. C., Rosolowsky E. W., Sternberg A., 2022, arXiv e-prints, p. arXiv:2203.09570
 Chon S., Omukai K., Schneider R., 2021, *MNRAS*, **508**, 4175
 Crowther P. A., Schnurr O., Hirschi R., Yusof N., Parker R. J., Goodwin S. P., Kissim H. A., 2010, *MNRAS*, **408**, 731
 Dale J. E., Ercolano B., Bonnell I. A., 2012, *MNRAS*, **427**, 2852
 Dale J. E., Ercolano B., Bonnell I. A., 2013, *MNRAS*, **430**, 234
 Decataldo D., Lupi A., Ferrara A., Pallottini A., Fumagalli M., 2020, *MNRAS*, **497**, 4718
 Dobbs C. L., Liow K. Y., Rieder S., 2020, *MNRAS*, **496**, L1
 Dobbs C. L., Bending T. J. R., Pettitt A. R., Bate M. R., 2022, *MNRAS*, **509**, 954
 Draine B. T., 2011, Physics of the Interstellar and Intergalactic Medium
 Fall S. M., Rees M. J., 1985, *ApJ*, **298**, 18
 Fall S. M., Krumholz M. R., Matzner C. D., 2010, *ApJ*, **710**, L142
 Figer D. F., 2005, *Nature*, **434**, 192
 Finkelstein S. L., et al., 2022, arXiv e-prints, p. arXiv:2207.12474
 Fujii M. S., Portegies Zwart S., 2016, *ApJ*, **817**, 4
 Fujii M. S., Saitoh T. R., Hirai Y., Wang L., 2021, *PASJ*, **73**, 1
 Fukushima H., Yajima H., 2021, *MNRAS*, **506**, 5512
 Fukushima H., Yajima H., 2022, *MNRAS*, **511**, 3346
 Fukushima H., Hosokawa T., Chiaki G., Omukai K., Yoshida N., Kuiper R., 2020a, *MNRAS*, **497**, 829
 Fukushima H., Yajima H., Sugimura K., Hosokawa T., Omukai K., Matsumoto T., 2020b, *MNRAS*, **497**, 3830
 Gavagnin E., Bleuler A., Rosdahl J., Teyssier R., 2017, *MNRAS*, **472**, 4155
 Geen S., Hennebelle P., Tremblin P., Rosdahl J., 2016, *MNRAS*, **463**, 3129
 Geen S., Soler J. D., Hennebelle P., 2017, *MNRAS*, **471**, 4844
 Gieles M., Portegies Zwart S. F., Baumgardt H., Athanassoula E., Lamers H. J. G. L. M., Sipior M., Leenaarts J., 2006, *MNRAS*, **371**, 793
 Gnedin O. Y., Lee H. M., Ostriker J. P., 1999, *ApJ*, **522**, 935
 González-Samaniego A., Vazquez-Semadeni E., 2020, *MNRAS*, **499**, 668
 Grudić M. Y., Hopkins P. F., Faucher-Giguère C.-A., Quataert E., Murray N., Kereš D., 2018, *MNRAS*, **475**, 3511
 Grudić M. Y., Kruijssen J. M. D., Faucher-Giguère C.-A., Hopkins P. F., Ma X., Quataert E., Boylan-Kolchin M., 2021, *MNRAS*, **506**, 3239
 Grudić M. Y., Guszejnov D., Offner S. S. R., Rosen A. L., Raju A. N., Faucher-Giguère C.-A., Hopkins P. F., 2022, *MNRAS*, **512**, 216
 Guszejnov D., Grudić M. Y., Offner S. S. R., Faucher-Giguère C.-A., Hopkins P. F., Rosen A. L., 2022, arXiv e-prints, p. arXiv:2205.10413
 Haghia H., Khalaj P., Hasani Zonoozi A., Kroupa P., 2017, *ApJ*, **839**, 60
 Hainich R., Ramachandran V., Shenar T., Sander A. A. C., Todt H., Gruner D., Oskinova L. M., Hamann W. R., 2019, *A&A*, **621**, A85
 Harikane Y., et al., 2022a, *ApJS*, **259**, 20
 Harikane Y., et al., 2022b, *ApJ*, **929**, 1
 Hasegawa K., Umemura M., Kitayama T., 2009, *MNRAS*, **397**, 1338
 He C.-C., Ricotti M., Geen S., 2019, *MNRAS*, **489**, 1880
 Hosek Matthew W. J., Lu J. R., Anderson J., Najjar F., Ghez A. M., Morris M. R., Clarkson W. I., Albers S. M., 2019, *ApJ*, **870**, 44
 Howard C. S., Pudritz R. E., Harris W. E., 2017, *MNRAS*, **470**, 3346
 Inayoshi K., Harikane Y., Inoue A. K., Li W., Ho L. C., 2022, *ApJ*, **938**, L10
 Inoguchi M., Hosokawa T., Mineshige S., Kim J.-G., 2020, *MNRAS*, **497**, 5061
 Inoue T., Inutsuka S.-i., 2012, *ApJ*, **759**, 35
 Isobe Y., Ouchi M., Nakajima K., Harikane Y., Ono Y., Xu Y., Zhang Y., Umeda H., 2023, arXiv e-prints, p. arXiv:2301.06811
 Kalari V. M., Horch E. P., Salinas R., Vink J. S., Andersen M., Bestenlehner J. M., Rubio M., 2022, arXiv e-prints, p. arXiv:2207.13078
 Kim J.-G., Kim W.-T., Ostriker E. C., 2016, *ApJ*, **819**, 137
 Kim J.-G., Kim W.-T., Ostriker E. C., 2018, *ApJ*, **859**, 68
 Kim J.-G., Ostriker E. C., Filippova N., 2021, *ApJ*, **911**, 128
 Kimm T., Bieri R., Geen S., Rosdahl J., Blaizot J., Michel-Dansac L., Garel T., 2022, *ApJS*, **259**, 21
 Kobayashi M. I. N., Inoue T., Inutsuka S.-i., Tomida K., Iwasaki K., Tanaka K. E. I., 2020, *ApJ*, **905**, 95
 Kroupa P., 2002, *Science*, **295**, 82
 Kroupa P., Aarseth S., Hurley J., 2001, *MNRAS*, **321**, 699
 Kruijssen J. M. D., 2012, *MNRAS*, **426**, 3008
 Kruijssen J. M. D., 2019, *MNRAS*, **486**, L20
 Kruijssen J. M. D., et al., 2019, *Nature*, **569**, 519
 Krumholz M. R., Matzner C. D., 2009, *ApJ*, **703**, 1352
 Krumholz M. R., Fumagalli M., da Silva R. L., Rendahl T., Parra J., 2015, *MNRAS*, **452**, 1447

- Krumholz M. R., McKee C. F., Bland-Hawthorn J., 2019, *ARA&A*, **57**, 227
 Kundic T., Ostriker J. P., 1995, *ApJ*, **438**, 702
 Lada C. J., Lada E. A., 2003, *ARA&A*, **41**, 57
 Lada C. J., Margulis M., Dearborn D., 1984, *ApJ*, **285**, 141
 Lahén N., Naab T., Johansson P. H., Elmegreen B., Hu C.-Y., Walch S., 2019, *ApJ*, **879**, L18
 Lancaster L., Ostriker E. C., Kim J.-G., Kim C.-G., 2021a, *ApJ*, **914**, 89
 Lancaster L., Ostriker E. C., Kim J.-G., Kim C.-G., 2021b, *ApJ*, **914**, 90
 Lancaster L., Ostriker E. C., Kim J.-G., Kim C.-G., 2021c, *ApJ*, **922**, L3
 Larsen S. S., Romanowsky A. J., Brodie J. P., Wasserman A., 2020, *Science*, **370**, 970
 Lejeune T., Cuisinier F., Buser R., 1997, *A&AS*, **125**, 229
 Leroy A. K., et al., 2018, *ApJ*, **869**, 126
 Li H., Vogelsberger M., Marinacci F., Gnedin O. Y., 2019, *MNRAS*, **487**, 364
 Lu J. R., Do T., Ghez A. M., Morris M. R., Yelda S., Matthews K., 2013, *ApJ*, **764**, 155
 Maeda R., Inoue T., Fukui Y., 2021, *ApJ*, **908**, 2
 Maia F. F. S., Moraux E., Joncour I., 2016, *MNRAS*, **458**, 3027
 Marigo P., et al., 2017, *ApJ*, **835**, 77
 Marks M., Kroupa P., Dabringhausen J., Pawłowski M. S., 2012, *MNRAS*, **422**, 2246
 Martin N. F., et al., 2022, *Nature*, **601**, 45
 Matsumoto T., 2007, *PASJ*, **59**, 905
 Matsumoto T., Dobashi K., Shimoikura T., 2015, *ApJ*, **801**, 77
 Matzner C. D., 2002, *ApJ*, **566**, 302
 McKenzie M., Bekki K., 2021, *MNRAS*, **500**, 4578
 Menon S. H., Federrath C., Krumholz M. R., 2022, *MNRAS*, **517**, 1313
 Murray N., Quataert E., Thompson T. A., 2010, *ApJ*, **709**, 191
 Myers P. C., Dame T. M., Thaddeus P., Cohen R. S., Silverberg R. F., Dwek E., Hauser M. G., 1986, *ApJ*, **301**, 398
 Osterbrock D. E., 1989, Astrophysics of gaseous nebulae and active galactic nuclei
 Pastorelli G., et al., 2019, *MNRAS*, **485**, 5666
 Pastorelli G., et al., 2020, *MNRAS*, **498**, 3283
 Peebles P. J. E., Dicke R. H., 1968, *ApJ*, **154**, 891
 Pfalzner S., 2009, *A&A*, **498**, L37
 Portegies Zwart S. F., McMillan S. L. W., Gieles M., 2010, *ARA&A*, **48**, 431
 Pouteau Y., et al., 2022, arXiv e-prints, p. arXiv:2203.03276
 Puzia T. H., Kissler-Patig M., Thomas D., Maraston C., Saglia R. P., Bender R., Goudfrooij P., Hempel M., 2005, *A&A*, **439**, 997
 Raskutti S., Ostriker E. C., Skinner M. A., 2016, *ApJ*, **829**, 130
 Ricotti M., Parry O. H., Gnedin N. Y., 2016, *ApJ*, **831**, 204
 Roman-Duval J., Jackson J. M., Heyer M., Rathborne J., Simon R., 2010, *ApJ*, **723**, 492
 Rosdahl J., Blaizot J., Aubert D., Stranex T., Teyssier R., 2013, *MNRAS*, **436**, 2188
 Sadanari K. E., Omukai K., Sugimura K., Matsumoto T., Tomida K., 2021, *MNRAS*, **505**, 4197
 Sadanari K. E., Omukai K., Sugimura K., Matsumoto T., Tomida K., 2023, *MNRAS*, **519**, 3076
 Salpeter E. E., 1955, *ApJ*, **121**, 161
 Schneider F. R. N., et al., 2018, *Science*, **359**, 69
 Sharda P., Federrath C., Krumholz M. R., 2020, *MNRAS*, **497**, 336
 Sharda P., Federrath C., Krumholz M. R., Schleicher D. R. G., 2021, *MNRAS*, **503**, 2014
 Shukrgaliyev B., Parmentier G., Berczik P., Just A., 2017, *A&A*, **605**, A119
 Skinner M. A., Ostriker E. C., 2015, *ApJ*, **809**, 187
 Spitzer L., 1987, Dynamical evolution of globular clusters
 Stacy A., McKee C. F., Lee A. T., Klein R. I., Li P. S., 2022, *MNRAS*, **511**, 5042
 Sugimura K., Matsumoto T., Hosokawa T., Hirano S., Omukai K., 2020, *ApJ*, **892**, L14
 Tang J., Bressan A., Rosenfield P., Slemer A., Marigo P., Girardi L., Bianchi L., 2014, *MNRAS*, **445**, 4287
 Toyouchi D., Inayoshi K., Ishigaki M. N., Tominaga N., 2022, *MNRAS*, **512**, 2573
 Tsuge K., Tachihara K., Fukui Y., Sano H., Tokuda K., Ueda J., Iono D., 2021, *PASJ*, **73**, 417
 Vanzella E., et al., 2017, *MNRAS*, **467**, 4304
 Vanzella E., et al., 2019, *MNRAS*, **483**, 3618
 Vanzella E., et al., 2022, arXiv e-prints, p. arXiv:2208.00520
 Vázquez-Semadeni E., Colín P., Gómez G. C., Ballesteros-Paredes J., Watson A. W., 2010, *ApJ*, **715**, 1302
 Wan Z., et al., 2020, *Nature*, **583**, 768
 Wang L., Kroupa P., Takahashi K., Jerabkova T., 2020, *MNRAS*, **491**, 440
 Wang L., Fujii M. S., Tanikawa A., 2021, *MNRAS*, **504**, 5778
 Weaver R., McCray R., Castor J., Shapiro P., Moore R., 1977, *ApJ*, **218**, 377
 Weidner C., Kroupa P., 2004, *MNRAS*, **348**, 187
 Williams J. P., McKee C. F., 1997, *ApJ*, **476**, 166
 Yajima H., et al., 2022, *MNRAS*, **509**, 4037
 Zonoozi A. H., Haghi H., Kroupa P., 2016, *ApJ*, **826**, 89
 da Silva R. L., Fumagalli M., Krumholz M., 2012, *ApJ*, **745**, 145

APPENDIX A: THRESHOLD SURFACE DENSITY OF GLOBULAR CLUSTER FORMATION

We summarize the underlying physics in massive star cluster formation under radiative feedback as described in [Fukushima & Yajima \(2021\)](#). We consider an expanding shell around an HII region. The equation of motion is described as ([Matzner 2002](#); [Krumholz & Matzner 2009](#))

$$\frac{d}{dt} (M_{\text{sh}} \dot{r}_{\text{sh}}) = 4\pi r_{\text{sh}}^2 \rho_i c_i^2, \quad (\text{A1})$$

where ρ_i and c_i are the density and the sound speed in HII regions. Here, we consider the contribution from the thermal pressure of ionized gas alone and ignore other effects, such as radiation pressure and gravitational force from stars. When the photon production rate balances with the total recombination rate in the HII region, the number density of HII regions is evaluated as

$$n_i = \left(\frac{\rho_i c_i^2}{k_B T_i} \right) = \left(\frac{3S_{\text{ion}}}{4\pi r_{\text{sh}}^3 \alpha_B} \right)^{1/2}, \quad (\text{A2})$$

where T_i , S_{ion} , and α_B are the temperature of ionized gas, the emissivity of ionizing photons, and the recombination coefficient $\alpha_B = 2.6 \times 10^{-13} (T_i / 10^4 \text{ K})^{-0.8} \text{ cm}^3 \text{s}^{-1}$ ([Osterbrock 1989](#)). Here, we assume that the gas is converted into stars with the constant conversion rates ϵ_* after the shell passes. The mass of expanding shell and the formed stars inside the shell are given as

$$M_{\text{sh}} = M_{\text{cl}} (1 - \epsilon_*) (r_{\text{sh}} / R_{\text{cl}})^3, \quad (\text{A3})$$

and

$$M_* = M_{\text{cl}} \epsilon_* (r_{\text{sh}} / R_{\text{cl}})^3. \quad (\text{A4})$$

The emissivity of ionizing photons is estimated as

$$S_{\text{ion}} = s_* M_*, \quad (\text{A5})$$

where s_* is the emissivity per unit mass. Here, we adopt the following dimensionless parameters

$$x = r_{\text{sh}} / R_{\text{cl}}, \quad (\text{A6})$$

and

$$\tau = \sqrt{3}t / t_{\text{HII}}, \quad (\text{A7})$$

where

$$t_{\text{HII}} = \left(\frac{1 - \epsilon_*}{\epsilon_*} \right)^{1/4} \left(\frac{3\alpha_B}{4s_* k_B^2 T_i^2} \right)^{1/4} \left(\frac{M_{\text{cl}}^3}{\pi^3 \Sigma_{\text{cl}}} \right)^{1/8}, \quad (\text{A8})$$

Substituting equation (A2), (A6), (A7) into equation (A1), the equation of shell motion is rewritten as

$$\frac{d}{d\tau} \left(x^3 \dot{x} \right) = x^2. \quad (\text{A9})$$

The self-similar solution of equation (A9) is found as $x = \tau/\sqrt{3}$ and $\dot{x} = 1/\sqrt{3}$ (Fukushima & Yajima 2021). Thus, the shell arrives at the outer edge of the cloud within the timescale of t_{HII} . We assume that the shell expansion time of t_{HII} is equal to the duration time of the star formation. The total stellar mass formed inside the cloud is given as

$$M_* = \epsilon_* M_{\text{cl}} = \dot{M}_* t_{\text{HII}}. \quad (\text{A10})$$

The star formation rates are expressed as

$$\dot{M}_* = \epsilon_{\text{ff}} \frac{M_{\text{cl}}}{t_{\text{ff}}}, \quad (\text{A11})$$

where $t_{\text{ff}} = \sqrt{3\pi/(32G\rho)}$ is the free-fall time of the cloud. Substituting equations (A8) and (A11) into equation (A10), we obtain the SFE as

$$\epsilon_* \simeq 0.07 \left(\frac{\epsilon_{\text{ff}}}{0.03} \right)^{4/5} \left(\frac{\Sigma_{\text{cl}}}{10^3 M_{\odot} \text{pc}^{-2}} \right)^{1/2} \left(\frac{M_{\text{cl}}}{10^6 M_{\odot}} \right)^{1/10} \left(\frac{T_i}{3 \times 10^4 \text{ K}} \right)^{-14/25} \left(\frac{s_*}{5.8 \times 10^{46} M_{\odot}^{-1} \text{s}^{-1}} \right)^{-1/5} \quad (\text{A12})$$

The shell expansion velocity does not depend on the radial position. With the SFE given as equation (A12), the shell velocity is calculated as

$$\begin{aligned} v_{\text{exp}} &= \frac{R_{\text{cl}}}{t_{\text{HII}}} \\ &\simeq 5.8 \text{ km/s} \left(\frac{\epsilon_{\text{ff}}}{0.03} \right)^{1/5} \left(\frac{\Sigma_{\text{cl}}}{10^3 M_{\odot} \text{pc}^{-2}} \right)^{-1/4} \left(\frac{M_{\text{cl}}}{10^6 M_{\odot}} \right)^{3/20} \\ &\quad \left(\frac{T_i}{3 \times 10^4 \text{ K}} \right)^{14/25} \left(\frac{s_*}{5.8 \times 10^{46} M_{\odot}^{-1} \text{s}^{-1}} \right)^{1/5}. \end{aligned} \quad (\text{A13})$$

The formed stars start to be bound when the total stellar mass exceeds 0.1 times the cloud mass (Fukushima & Yajima 2021). At this epoch, ionizing fronts propagate beyond the star cluster. When the thermal pressure on the shell overcomes the gravitational force, the gas around the star clusters is dispersed. On the other hand, the dense gas remains, and HII regions are confined if the gravitational force is strong enough to hold the ionized gas. In such a case, the gas keeps accreting onto the star cluster and contributes to further star formation. As a result, the high-density stellar core forms. Assuming that the expanding shell around the star cluster has the same velocity as the semi-analytical solution of equation (A13), the condition for binding the shell is given as

$$v_{\text{exp}} < v_{\text{esc}} = \sqrt{2GM_{\text{core}}/R_{\text{core}}}, \quad (\text{A14})$$

where M_{core} and R_{core} are the core mass and radius. These values are typically $R_{\text{core}} \sim 0.1R_{\text{cl}}$ and $M_{\text{core}} \sim 10^{-2} M_{\text{cl}}$. We obtain the conditions for the formation of a massive star cluster as

$$\begin{aligned} \Sigma_{\text{cl}} > \Sigma_{\text{thr}} &= 750 M_{\odot} \text{pc}^{-2} \left(\frac{\epsilon_{\text{ff}}}{0.03} \right)^{2/5} \left(\frac{M_{\text{cl}}}{10^6 M_{\odot}} \right)^{-1/5} \\ &\quad \left(\frac{T_i}{2.5 \times 10^4 \text{ K}} \right)^{28/25} \left(\frac{s_*}{1.1 \times 10^{47} M_{\odot}^{-1} \text{s}^{-1}} \right)^{2/5}. \end{aligned} \quad (\text{A15})$$

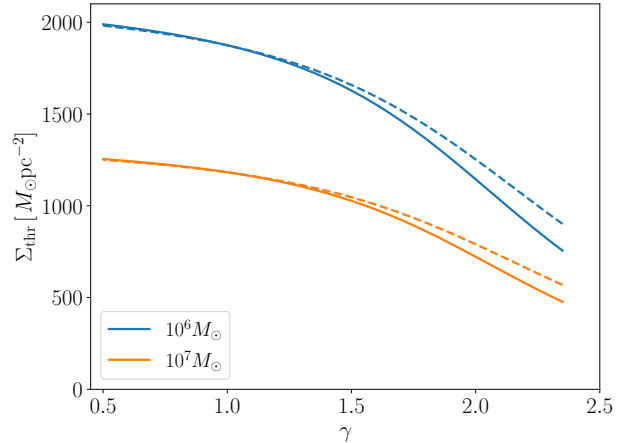


Figure A1. The threshold surface density (Σ_{thr}) as the function of the slope of the IMF (γ). Each line shows the cases with the cloud of $M_{\text{cl}} = 10^6 M_{\odot}$ (blue) and $10^7 M_{\odot}$ (orange). The solid (dashed) line shows the cases that the maximum stellar mass is $300 M_{\odot}$ ($150 M_{\odot}$).

In this study, we do not include magnetic fields. If strong magnetic fields exist, star formation rates decrease (e.g., Kim et al. 2021). The threshold value of equation (A15) depends on star formation rates as $\Sigma_{\text{thr}} \propto \epsilon_{\text{ff}}^{2/5}$. If ϵ_{ff} is reduced to half by magnetic fields, the condition of young massive star cluster formation is relaxed as $\Sigma_{\text{thr}} \sim 570 M_{\odot} \text{pc}^{-2}$.

Combining the emissivity of ionizing photons as shown in Figure 1, we calculate the threshold surface densities as the function of the power-law index of the IMF (γ). Figure A1 shows the values of Σ_{thr} as a function of γ in the clouds with $M_{\text{cl}} = 10^6 M_{\odot}$ and $10^7 M_{\odot}$. In both cases, the threshold surface densities are less than $10^3 M_{\odot} \text{pc}^{-2}$ for the standard IMF ($\gamma \sim 2.35$). At $\gamma \gtrsim 1.5$, the values of Σ_{thr} are larger than $\sim 10^3 M_{\odot} \text{pc}^{-2}$ of which clouds are rare in observations of local galaxies (e.g., Roman-Duval et al. 2010). We also consider the dependence of Σ_{thr} on the maximum stellar mass (M_{max}) of the IMF. The dot and dashed lines in Figure A1 show the cases that the maximum stellar masses are $M_{\text{max}} = 300 M_{\odot}$ and $150 M_{\odot}$ with the Salpeter IMF. At $\gamma < 1.5$, the values of Σ_{thr} depend on the maximum stellar mass. However, the threshold surface density does not vary with the maximum stellar mass at $\gamma > 1.5$.

This paper has been typeset from a TeX/LaTeX file prepared by the author.